Chapter 4

A Contact Dynamics Formulation

4.1 Introduction

In this chapter, we describe a contact dynamics (CD) approach to our NURBS-based discrete method. By combining particle shape flexibility through NURBS, properties of implicit time integration (e.g., larger time steps) and non-penetrating constraints, as well as a reduction to a static formulation in the limit of an infinite time step, we target applications in which the classical discrete element method either performs poorly or simply fails, i.e., in granular systems composed of rigid or highly stiff angular particles and subjected to quasi-static or dynamic flow conditions. The integration of CD and our NURBS-based discrete method is made possible while significantly simplifying implementation and maintaining comparable performance with existing CD approaches.

To motivate the development of our approach, we first refer the reader to Table 4.1 for a brief summary of the key features of and differences between CD and the classical DEM by Cundall and Strack [24]. In the following, we highlight the difficulties associated with classic CD and DEM followed by a description on how we eliminate them through the combined approach.

The so-called Non-Smooth CD, originally developed by Moreau [61; 62; 102; 103], is an alternative discrete approach to the DEM. The most prominent feature of CD, in contrast to that of classical DEM, is that the particles are considered perfectly rigid and the contact forces are determined as those that prevent interparticle penetration and at the same time satisfy the frictional stick-slip constraints. In their simplest forms, these contact laws are embodied in the so-called Signorini unilateral contact condition and classical Coulomb law, as shown in Figures 2.2a and 2.2b, respectively. Commensurate with these physical

Table 4.1: Comparison of Non-Smooth Contact Dynamics and classical DEM

Feature	Non-Smooth Contact Dynamics	Classic DEM
Normal contact	Rigid; unilateral contact[1,2] or non-penetration constraint directly included	Modeled using normal spring; particles overlap
Friction contact	Stick-slip frictional constraint[1,2] directly included	Imposes shear force incrementally using relative velocity from previous step
Time integration	Implicit, usually stable, and with larger time step[3]	Explicit, with stability criterion; critical time step scales with inverse of spring frequency. Inefficient for highly stiff particles and cannot be applied to rigid particles
Collision response	Considers collisions and stick-slip frictional transitions simultaneously; velocities may be non-smooth	No real collisions and velocity jumps cannot occur due to continuous nature of contact spring
Damping	Numerical damping[4]	Through global and/or local damping devices, i.e., dashpots
Quasistatic limit	Can be directly included in formulation	Dynamic in nature; oscillations in solutions are typical; quasistatic limit is approached using global and/or local damping
Particle morphology representation[5,6]	Disk- or sphere-clustering and polyhedra	
Implementation difficulty	Intermediate to difficult[7]	Easy
Computational efficiency	Contact and constraint forces solved implicitly. Geometrical information (e.g., gap values and contact orientations) are stored in matrices as part of the solution procedure; higher memory requirement[8]	Contact forces are solved explicitly using particle overlap and previous velocities; time integration easily parallelized. Minimal storage of geometrical information; lower memory requirement

(1) Regularization to account for particle elasticity possible (e.g., [99])
(2) See Figure 2.2
(3) Although the time step can be larger, it has to be reasonable so that collisions are properly resolved
(4) Does not apply in the quasistatic limit
(5) We list only those approaches, beyond ellipses/ellipsoids, that appear to be currently most widely applied
(6) Improved using NURBS in this work
(7) Made easier in this work
(8) In this work, managed using efficient large-scale mathematical programming solvers (e.g., [100; 101])

enhancements, however, is the need for both contact and constraint forces to be solved simultaneously or implicitly since the problem is nonlinear. The need for an implicit solution procedure till today remains the primary reason why CD is deemed much more complicated to implement than DEM. This has thwarted the wide adoption of CD despite the favorable performance that has been shown through a number of studies [73–83].

While there is wide applicability of DEM, its application has gone beyond its restriction as a tool that is strictly applicable only to materials with finite elasticity. For example, DEM is widely used as a tool to study real granular materials that are almost rigid or highly stiff in nature. Here, finite elasticity means that the contact interaction is essentially modeled using springs. Under explicit time integration algorithms that are typically used in DEM, the stable time step is restricted by the critical time step, which scales with the inverse of the contact spring-particle mass frequency. This results in infinitesimally small time steps if material parameters corresponding to highly stiff particles (e.g., rocks, sand, steel) are used. Although explicit integration algorithms can be easily parallelized, the runtime for stiff systems remains computationally prohibitive. One modeling technique commonly employed in practice to overcome this restriction is to simply reduce the contact stiffness, usually by two to four orders of magnitude, to the extent that particle kinematics obtained from simulations are still somewhat representative of the overall response of the actual system of interest. If quasi-static behavior is assumed to hold, usually used in combination with stiffness tuning is mass scaling, in which the particle masses are adjusted (usually increased) such that the combined spring-particle system frequency is lowered, increasing the time step size. In practice, model calibration by means of mass scaling and/or stiffness tuning is a delicate and cumbersome process. Another problem that is associated with the presence of contact springs and the dynamic nature of DEM is the introduction of unwanted oscillations or noise, with frequencies that increase with spring stiffness. This requires additional calibration of the global and/or local damping parameters. Moreover, under certain loading conditions (e.g., strain-controlled and dynamic), either particle kinematics or contact forces obtained under such calibration procedures can be highly inaccurate [57].

Recent CD approaches include techniques to represent complex particle morphology or shape, and these have been described in Chapter 2. In this aspect, recent trends show a clear dichotomy between the choice of shape representation technique. A key component in the CD formulation is the signed separation or gap, which is used in the determination of constraint forces to prevent particle interpenetration. While the polyhedra approach is considered a more accurate shape representation technique than the clustering approach, the associated algorithms for the determination of the signed penetration are complicated due to the need to enumerate all the various combinations of contact entities (node, edge, surface). As such, the simpler disk/sphere-clustering is favored over the more accurate polyhedra-based approach.

We combine and refine two important developments that allow us to eliminate all the above difficulties:

- We simplify the formulation and implementation of CD significantly by generalizing a variational CD formulation recently developed for disks and spheres [72; 99; 104]. This particular formulation, which is employed here, is appealing because it provides a way for CD to be easily implemented and solved using off-the-shelf mathematical programming solvers. The most prominent advantage of this formulation is its automatic inclusion of the quasi-static limit, enabling quasi-static modeling without the need for adjusting damping parameters or time step.

- We remove the complexities associated with polyhedra-based contact detection algorithms by adopting NURBS to describe arbitrary particle geometries. Following the approach as described in Chapter 3 to determine the signed gap, the integration of our NURBS-based discrete method into the CD formulation is shown to be simple and straightforward. The 'knot-to-surface' approach to contact described in Chapter 3 is similar to that employed in the contact treatment of frictionless bodies in isogeometric analysis [93]. The key difference and novelty here is on the simultaneous treatment of contact elasticity and frictional contact within the aforementioned CD formulation, as well as the ability to perform contact calculations for granular systems, which contain a large number of particles. Both particle elasticity and friction at the contact level are treated implicitly and simultaneously, and the contact algorithm is cast into a mathematical programming-based contact dynamics framework.

This chapter describes the details of how each of the above items is implemented and is structured as follows: we describe the contact problem and summarize the variational formulation of the general contact problem for frictional particles in Section 4.2; then, we present two numerical examples in Section 4.4 to demonstrate the capabilities of the combined approach before closing in Section 4.5. For clarity of presentation and implementation details, we limit our discussion to the two-dimensional case. An extension of the method to the three-dimensional setting is outlined in Appendix B.

4.2 Governing Equations for Frictional and Arbitrary-Shaped Particles

The formulations from [51; 72; 99; 104] carry forward completely to the general case of frictional and arbitrary-shaped particles without any change. As such, simplicity of implementation is retained. Here, we present a summary containing only those key equations required for the completeness of presentation. Where necessary, we point the reader to the appropriate references for further details.

4.2.1 General contact problem definition

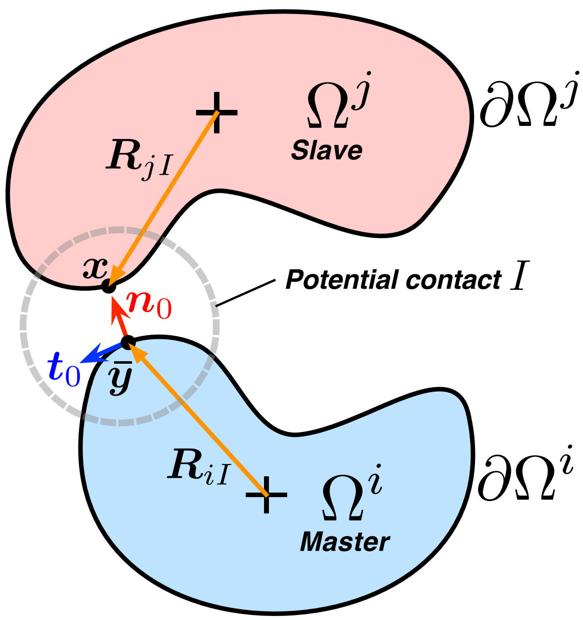

Figure 4.1: Illustration of the problem of contact between two particles (Ω^i and Ω^j) at time t_0. See text for a description of the associated quantities.

For convenience, we repeat here the contact problem described in Chapter 3, specialized to the 2D case as shown in Figure 4.1. The two-particle contact problem is defined at some initial time initial time t_0. Let W_i be the set of potential contacts associated with particle i and denote by $I \in W_i$ a particular contact point in the set. A contact point on the slave particle Ω^j is denoted by $\boldsymbol{x}$, while the contact point on the master particle is defined as the closest point projection of $\boldsymbol{x}$ onto the boundary of the master particle:

$$\bar{\boldsymbol{y}} \equiv \bar{\boldsymbol{y}}(\boldsymbol{x}) = \min_{\boldsymbol{y} \in \partial\Omega^i} \|\boldsymbol{x} - \boldsymbol{y}\| \tag{4.1}$$

As shown in Figure 4.1, the contact plane at a potential contact point I is described on the master boundary $\partial\Omega^i$ by the normal $\boldsymbol{n}_0$ and tangent $\boldsymbol{t}_0$ at point $\bar{\boldsymbol{y}}$. The gap at time t_0 is then defined as

$$g_0(\boldsymbol{x}) = (\boldsymbol{x} - \bar{\boldsymbol{y}}(\boldsymbol{x}))^T \, \boldsymbol{n}_0 \tag{4.2}$$

with the non-penetration constraint requiring that $g \geq 0$.

4.2.2 Notation for general multi-particle system

To facilitate the variational formulation of the governing equations, we first set the notation for the general multi-particle system that will be used throughout this chapter. A particle i has mass m^i and mass moment of inertia J^i. The position and rotation of the particle are denoted by $\boldsymbol{x}^i = (x^i, y^i)^T$ and α^i, respectively, and their corresponding translational and rotational velocities by $\boldsymbol{v}^i = (v^i_x, v^i_y)^T$ and ω^i. We introduce the following matrix or vector quantities that cover general n-particle systems:

$$\begin{aligned}
&\boldsymbol{M} = \mathrm{diag}(m^1, m^1, \ldots, m^n, m^n) \\
&\boldsymbol{J} = \mathrm{diag}(J^1, \ldots, J^n) \\
&\boldsymbol{x} = (\boldsymbol{x}^1, \ldots, \boldsymbol{x}^n), \boldsymbol{v} = (\boldsymbol{v}^1, \ldots, \boldsymbol{v}^n) \\
&\boldsymbol{\alpha} = (\alpha^1, \ldots, \alpha^n), \boldsymbol{\omega} = (\omega^1, \ldots, \omega^n) \\
&\boldsymbol{g} = (g^1, \ldots, g^N), \boldsymbol{p} = (p^1, \ldots, p^N), \boldsymbol{q} = (q^1, \ldots, q^N)
\end{aligned} \tag{4.3}$$

where $\boldsymbol{M}$ is the diagonal matrix containing the particle masses and $\boldsymbol{J}$ is the diagonal matrix containing the particle mass moments of inertia. The kinematical quantities are the vectors of particle translations $\boldsymbol{x}$ and rotations $\boldsymbol{\alpha}$, and their corresponding velocities $\boldsymbol{v}$ and $\boldsymbol{\omega}$. The contact quantities are given by the vectors $\boldsymbol{p}$, $\boldsymbol{q}$, and $\boldsymbol{g}$, which are the contact normal forces, shear forces, and gap values, respectively, each at N number of contacts.

A quantity, which at the initial time is denoted by $\square_0$, would then be denoted at time

$t_0 + \Delta t$ by $\Box$. For example, $\boldsymbol{x}_0$ and $\boldsymbol{v}_0$ are the known positions and velocities at time t_0, while $\boldsymbol{x}$ and $\boldsymbol{v}$ are the corresponding quantities at time $t_0 + \Delta t$. With this notation, an increment of a quantity will be denoted by $\Delta\Box = \Box - \Box_0$.

4.2.3 Discrete update equations

Under the discretization of the equations of motion using the θ-method [105], the resulting discrete update equations for translation and rotations are given by:

$$\begin{aligned} \bar{\boldsymbol{M}}\Delta\boldsymbol{x} &= \bar{\boldsymbol{f}}_0 = \boldsymbol{f}_{\text{ext}} + \bar{\boldsymbol{M}}\boldsymbol{v}_0\Delta t \\ \bar{\boldsymbol{J}}\Delta\boldsymbol{\alpha} &= \bar{\boldsymbol{m}}_0 = \boldsymbol{m}_{\text{ext}} + \bar{\boldsymbol{J}}\boldsymbol{\omega}_0\Delta t \end{aligned} \tag{4.4}$$

In the above, the matrices $\bar{\boldsymbol{M}}$ and $\bar{\boldsymbol{J}}$ contain the scaled particle masses and mass moments of inertia, respectively:

$$\begin{aligned} \bar{\boldsymbol{M}} &= \frac{1}{\theta\Delta t^2}\boldsymbol{M} \\ \bar{\boldsymbol{J}} &= \frac{1}{\theta\Delta t^2}\boldsymbol{J} \end{aligned} \tag{4.5}$$

The effective translational force vector $\bar{\boldsymbol{f}}_0$ contains the external load vector $\boldsymbol{f}_{\text{ext}}$, which we have assumed to be constant (e.g., due to gravity). The effective rotational moment vector $\bar{\boldsymbol{m}}_0$ contains the external rotational moments $\boldsymbol{m}_{\text{ext}}$, which may be applied on the particles.

The translational and angular velocities are calculated, respectively, as

$$\begin{aligned} \boldsymbol{v} &= \frac{1}{\theta}\left[\frac{\Delta\boldsymbol{x}}{\Delta t} - (1-\theta)\boldsymbol{v}_0\right] \\ \boldsymbol{\omega} &= \frac{1}{\theta}\left[\frac{\Delta\boldsymbol{\alpha}}{\Delta t} - (1-\theta)\boldsymbol{\omega}_0\right] \end{aligned} \tag{4.6}$$

where $0 \leq \theta \leq 1$. The stability properties of the θ-method are well known: for $\theta = \frac{1}{2}$ an unconditionally stable and energy preserving scheme is recovered, for $\theta > \frac{1}{2}$ the scheme is unconditionally stable and dissipative, and for $\theta < \frac{1}{2}$ stability depends on the time step. In the context of binary collisions, the algorithmic energy dissipation that occurs for $\theta > \frac{1}{2}$ can be related to the physical dissipation associated with impact and thus to the restitution coefficient e through the relation

$$e = \frac{1-\theta}{\theta} \tag{4.7}$$

Indeed, as shown in [72], a value of $\theta = \frac{1}{2}$ corresponds to an elastic collision while $\theta = 1$ reproduces a perfectly inelastic collision. Binary elastic and plastic collision tests are shown in Appendix A.2.

4.2.4 Variational formulation of contact problem

Following the formulation procedure as described in [51; 72; 99; 104], the resulting discrete mixed force-displacement problem, including contact constraints, takes the form:

$$\begin{aligned}
\min_{\Delta\boldsymbol{x},\Delta\boldsymbol{\alpha}}\ \max_{\boldsymbol{p},\,\boldsymbol{q}}\quad & \left\{\tfrac{1}{2}\Delta\boldsymbol{x}^T\bar{\boldsymbol{M}}\Delta\boldsymbol{x} - \Delta\boldsymbol{x}^T\bar{\boldsymbol{f}}_0\right\} \\
& + \left\{\tfrac{1}{2}\Delta\boldsymbol{\alpha}^T\bar{\boldsymbol{J}}\Delta\boldsymbol{\alpha} - \Delta\boldsymbol{\alpha}^T\bar{\boldsymbol{m}}_0\right\} \\
& + \left\{\Delta\boldsymbol{x}^T(\boldsymbol{N}_0\,\boldsymbol{p} + \widehat{\boldsymbol{N}}_0\,\boldsymbol{q}) - \boldsymbol{g}_0^T\boldsymbol{p} - \Delta\boldsymbol{\alpha}^T\left(\boldsymbol{R}_0^q\,\boldsymbol{q} + \boldsymbol{R}_0^p\,\boldsymbol{p}\right)\right\} \\
& - \left\{\frac{1}{2}\boldsymbol{p}^T\boldsymbol{C}_N\boldsymbol{p} + \frac{1}{2}\Delta\boldsymbol{q}^T\boldsymbol{C}_T\Delta\boldsymbol{q}\right\} \\
\text{subject to}\quad & \|\boldsymbol{q}\| - \mu\boldsymbol{p} \leq \boldsymbol{0}, \quad \boldsymbol{p} \geq \boldsymbol{0}
\end{aligned} \tag{4.8}$$

With a slight abuse of notation, we have denoted the vector containing the absolute values of the shear forces by $\|\boldsymbol{q}\|$. The matrix $\boldsymbol{N}$ contains all the normals associated with potential contacts $\boldsymbol{n} = (n_x, n_y)^T$ while the matrix $\widehat{\boldsymbol{N}}$ has the same form contains entries $\boldsymbol{t} = (-n_y, n_x)^T$, i.e., the tangent vector defined as the 90° counterclockwise rotation of $\boldsymbol{n}$. We note the presence of the term with incremental shear $\Delta\boldsymbol{q} = \boldsymbol{q} - \boldsymbol{q}_0$, which requires the tracking of shear forces at contact points and makes the problem history-dependent.

In equation (4.8), the matrix $\boldsymbol{R}_0^q$ contains the contribution of the total angular momentum balance from the tangential forces and contains entries $\boldsymbol{R}_{iI}^T\boldsymbol{n}_0$ where $\boldsymbol{R}_{iI}$ is the moment arm vector extending from the centroid of particle i to the contact point $\bar{\boldsymbol{y}}$. The matrix $\boldsymbol{R}_0^p$ contains the contribution of the total angular momentum balance from the normal contact forces and contains entries $-\boldsymbol{R}_{iI}^T\boldsymbol{t}_0$. Both $\boldsymbol{R}_{iI}^T\boldsymbol{n}_0$ and $-\boldsymbol{R}_{iI}^T\boldsymbol{t}_0$ are signed moment arms and their signs depend on whether the associated contact force induces a positive (clockwise) or negative moment on the particle. A similar description applies to the slave particle using its contact normal $-\boldsymbol{n}_0$ and tangent $-\boldsymbol{t}_0$. The matrices $\boldsymbol{C}_N$ and $\boldsymbol{C}_T$ contain the compliances

$1/k_N$ and $1/k_T$ on the diagonal, where k_N and k_T are the normal and tangential contact stiffnesses, respectively. Finally, the Coulomb criterion is imposed with $\mu = \tan\phi$ being the effective interparticle friction coefficient and ϕ is the effective friction angle at the scale below the particle angularity level.

4.2.5 Optimality conditions

Following the approach in [72], the first-order KKT conditions associated with equation (4.8) give the linear moment balance:

$$\bar{\boldsymbol{M}}\Delta\boldsymbol{x} + \boldsymbol{N}_0\boldsymbol{p} + \widehat{\boldsymbol{N}}_0\boldsymbol{q} = \bar{\boldsymbol{f}}_0 \tag{4.9}$$

balance of angular momentum:

$$\bar{\boldsymbol{J}}\Delta\boldsymbol{\alpha} - \boldsymbol{R}_0^q\boldsymbol{q} - \boldsymbol{R}_0^p\boldsymbol{p} = \bar{\boldsymbol{m}}_0 \tag{4.10}$$

sliding friction conditions:

$$\|\boldsymbol{q}\| - \mu\boldsymbol{p} + \boldsymbol{s} = \boldsymbol{0}, \boldsymbol{s} \geq \boldsymbol{0} \tag{4.11}$$

$$\mathrm{diag}(\boldsymbol{s})\boldsymbol{\lambda} = \boldsymbol{0}, \boldsymbol{\lambda} \geq \boldsymbol{0} \tag{4.12}$$

where $\boldsymbol{s}$ is the slack vector, introduced to enforce equality, and kinematics:

$$\boldsymbol{N}_0^T\Delta\boldsymbol{x} + \mu\boldsymbol{\lambda} = \boldsymbol{g}_0 + \boldsymbol{C}_N\boldsymbol{p} \tag{4.13}$$

$$\widehat{\boldsymbol{N}}_0^T\Delta\boldsymbol{x} - (\boldsymbol{R}_0^{qT} + \boldsymbol{R}_0^{pT})\Delta\boldsymbol{\alpha} = \mathrm{sgn}(\boldsymbol{q})\boldsymbol{\lambda} + \boldsymbol{C}_T\Delta\boldsymbol{q} \tag{4.14}$$

where sgn is the signum function. The kinematics in equations (4.13) and (4.14) pertain to the associated sliding rule, which leads to an apparent dilation proportional to the friction coefficient μ. However, as described in [72], this dilation can be viewed as an artifact of the time discretization which, with the exception of a few pathological cases, is gradually reduced as the time step is reduced. Moreover, it was shown in [72] that the dilation, even for rather large time steps, is negligible over a range of common conditions, including both instances of highly dynamic and relatively unconfined flows as well as confined quasi-static deformation processes. The consequences of the associated sliding rule are discussed in

Appendix A.3.

4.2.6 Force-based problem

Finally, it is possible to cast equation (4.8) in terms of the following force based problem:

$$\begin{aligned}
\text{minimize} \quad & \frac{1}{2}\boldsymbol{r}^T\bar{\boldsymbol{M}}^{-1}\boldsymbol{r} + \frac{1}{2}\boldsymbol{t}^T\bar{\boldsymbol{J}}^{-1}\boldsymbol{t} + \boldsymbol{g}_0^T\boldsymbol{p} \\
& + \frac{1}{2}\boldsymbol{p}^T\boldsymbol{C}_N\boldsymbol{p} + \frac{1}{2}\Delta\boldsymbol{q}^T\boldsymbol{C}_T\Delta\boldsymbol{q} \\
\text{subject to} \quad & \boldsymbol{r} + \boldsymbol{N}_0\boldsymbol{p} + \widehat{\boldsymbol{N}}_0\boldsymbol{q} = \bar{\boldsymbol{f}}_0 \\
& \boldsymbol{t} - \boldsymbol{R}_0^q\,\boldsymbol{q} - \boldsymbol{R}_0^p\,\boldsymbol{p} = \bar{\boldsymbol{m}}_0 \\
& \|\boldsymbol{q}\| - \mu\boldsymbol{p} \leq \boldsymbol{0}, \quad \boldsymbol{p} \geq \boldsymbol{0}
\end{aligned} \tag{4.15}$$

where $\boldsymbol{t}$ is the dynamic vector associated with the rotations, i.e., torque vector.

4.2.7 Static limit

Omitting the dynamic forces $\boldsymbol{r}$ and $\boldsymbol{t}$ from equation (4.15) gives rise to the following static problem which is valid in the limit of Δt tending to infinity:

$$\begin{aligned}
\text{minimize} \quad & \boldsymbol{g}_0^T\boldsymbol{p} + \frac{1}{2}\boldsymbol{p}^T\boldsymbol{C}_N\boldsymbol{p} + \frac{1}{2}\Delta\boldsymbol{q}^T\boldsymbol{C}_T\Delta\boldsymbol{q} \\
\text{subject to} \quad & \boldsymbol{N}_0\boldsymbol{p} + \widehat{\boldsymbol{N}}_0\boldsymbol{q} = \bar{\boldsymbol{f}}_{\text{ext}} \\
& \boldsymbol{R}_0^q\,\boldsymbol{q} + \boldsymbol{R}_0^p\,\boldsymbol{p} = \boldsymbol{0} \\
& \|\boldsymbol{q}\| - \mu\boldsymbol{p} \leq \boldsymbol{0}, \quad \boldsymbol{p} \geq \boldsymbol{0}
\end{aligned} \tag{4.16}$$

The above principle is useful for quasi-static problems governed by an internal pseudo-time rather than physical time. Examples include common soil mechanics laboratory tests such as triaxial tests, quasi-static soil-structure interaction problems such as cone penetration, and various applications in the earth sciences where the time scales are such that the deformations are of a quasi-static nature (e.g., [106; 107]). We note that in the quasi-static formulation, the accuracy of the scheme would then depend on the increment size of the applied boundary conditions (e.g., wall displacements or stresses).

4.2.8 Solution procedure and computational complexity

We observe that equations (4.15) and (4.16) are essentially standard quadratic programming problems. In this work, the primal-dual interior-point solver in MOSEK [101] is used for the solution of both problems. The solution and storage costs associated with these problems are usually justified by the larger analysis steps that can be taken when using implicit algorithms. This is more so for systems comprised of rigid or highly stiff particles in which explicit solution procedures perform poorly or simply fail. Moreover, large-scale mathematical programming solvers with sparse storage (e.g., [100; 101]) are becoming widely available and increasingly efficient and robust. More recent solvers such as MOSEK [101] also include multi-core or multi-threaded capabilities.

The performance of the primal-dual interior-point method in the context of our proposed contact dynamics formulation has been described in detail in [72], and the following properties are summarized: 1) insensitivity of iteration count to problem size, 2) arithmetic complexity that is equivalent to standard Newton-Raphson schemes, and 3) highly robust (almost never fails or stalls). The overall cost is therefore comparable to implicit Newton-Raphson-type schemes used in nonlinear finite element analysis. For details on the fundamental theory and implementation of interior-point methods, we refer the reader to [108].

4.3 Contact Implementation

The CD formulation of either equation (4.15) or (4.16) described in the previous section offers great simplicity and significant effort reduction in contact implementation in that the only required information is the signed gap values at the initial time $\boldsymbol{g}_0$. The implementation of the contact algorithm proceeds as described in Chapter 3, specialized to the 2D case.

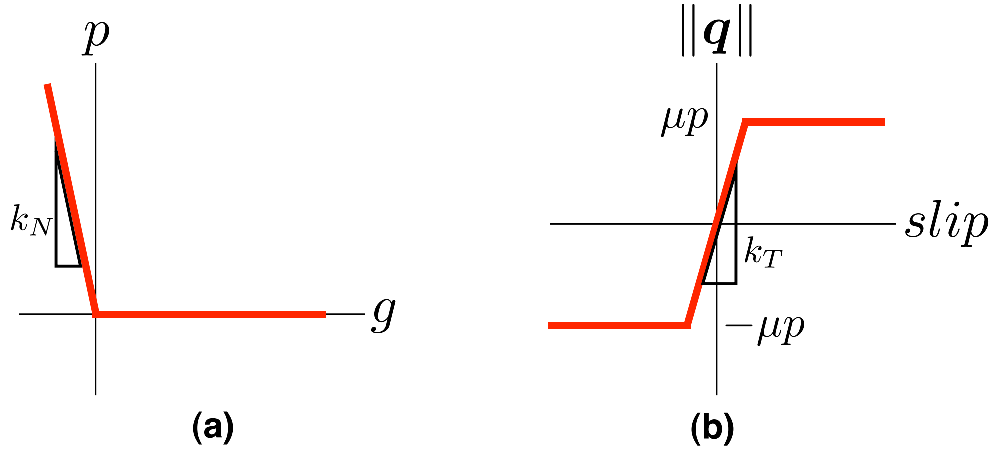

Figure 4.2: Linear elastic contact law: (a) normal reaction force p against separation or gap g and (b) friction force $\|\boldsymbol{q}\|$ against slip; μ is the friction coefficient.

Here, we have only considered the case of linear contact elasticity, as shown in Figure 4.2, but extension to nonlinear elasticity is entirely possible as is the consideration of more complex contact models incorporating hardening, viscous effects, etc. The resulting scheme bears some similarity to standard DEM schemes in that the consideration of a finite contact stiffness implies the possibility for an elastically reversible interparticle penetration. The inclusion of contact elasticity reproduces the more basic case of rigid particles in the limit of the contact stiffness tending to infinity. Moreover, in contrast to standard DEM, there are no algorithmic repercussions from operating with a large or, in the extreme case, infinite stiffness, reproducing the contact law shown in Figure 2.2. Indeed, the same algorithm is used regardless of the contact stiffness, with perfect rigidity being a limiting case that allows for certain simplifications. For example, in the limiting case, both $\boldsymbol{C}_N$ and $\boldsymbol{C}_T$ in either equation (4.15) or (4.16) are zero, and the associated quadratic terms drop out from the formulation. In particular, this means that no information of the shear forces needs to be carried over from one time step to the next. As a result, contact stiffness values that are representative of real materials (e.g., steel or rock) can be used without causing numerical difficulties.

The static problem described by equation (4.16) reveals a number of interesting properties related to the indeterminacy of force networks in granular media. It is well known that rigid particles lead to a situation where the force network solution is non-unique [109–112]. Setting $\boldsymbol{C}_N = \boldsymbol{C}_T = \mathbf{0}$ in equation (4.16) leads to a linear program where global optimality may be achieved by more than one set of forces. Conversely, for finite values of $\boldsymbol{C}_N$ and $\boldsymbol{C}_T$, the solution is unique, i.e., there is a unique set of contact forces leading to the optimal value of the objective function.

4.4 Numerical Examples

In this section, we present two examples that highlight the effects of particle morphology on the macroscopic response of granular assemblies, as well as the robustness of our proposed method. In particular, we compare responses of assemblies with three levels of particle angularity: disk, angular but (strictly) convex, and non-convex particles.

4.4.1 Biaxial compresion

Biaxial compression simulations using the static limit formulation in equation (4.16) are carried out on a rectangular assembly of initial width W_0 and initial height H_0 containing 1520 particles. First, an assembly with non-convex particles is prepared using 16 different shapes. Then, two additional assemblies — one with angular convex particles and another with disks — are also prepared. The particles in these assemblies are obtained by matching average particle diameters of the 16 non-convex shapes. Effectively, sphericity is kept constant and a comparison of effects of angularity is made. The three assemblies with their corresponding particle shapes are shown in Figure 4.3.

The non-convex and angular assemblies have an initial porosity of approximately 0.152, while the disk assembly has an initial porosity of approximately 0.176. The higher porosity of the disk assembly points to the inability of disks to match porosity by just simply matching average particle diameters. Indeed, a wider distribution of disk sizes would be required in this case to match the initial porosity of 0.152, which in turn would substantially increase the number of particles. In this regard, the use of disks to represent particle geometry introduces an unavoidable geometrical bias, which leads to packings with higher porosities [91]. Nevertheless, in this example, we retain the disk assembly for comparison with the other two assemblies. Two interparticle friction coefficients $\mu = 0.3$ and 0.5 are used to gauge the effect of interparticle friction. The upper wall is moved downwards while the applied stress on the right wall σ_3 is maintained at 125 units. A total of about 150 steps are used to impose a total axial strain of approximately 0.21. The left and bottom walls are stationary. All walls are frictionless.

To show the effects of particle elasticity, we perform the tests with several values of particle elasticity: $k_N = \infty$, 10^8, 10^6, 10^5. The tangential stiffness is set at $k_T = 2k_N/3$, which is within the range for a physically consistent volumetric response in granular materials [99; 113]. At every time step, the current width W and current height H of the assembly box are tracked, and the stresses σ_1 and σ_3 computed using the contact forces of the particles impinging on the top and right walls, respectively. The results in terms of deviatoric stress $\sigma_1 - \sigma_3$ versus axial strain, $\epsilon_a = 1 - H/H_0$, and volumetric strain, $\epsilon_v = 1 - WH/(W_0 H_0)$, versus axial strain are shown in Figures 4.4 through 4.7. We see that the macroscopic response at $k_N = 10^8$ is close to rigid. As k_N is lowered, a more elastic initial response is observed in which the sharp initial peak is progressively suppressed and the peak response lowers slightly. At $k_N = 10^5$, an initial slope in the deviatoric stress becomes visible and the corresponding volumetric strain response shows an initial compaction followed by volume expansion. The deformed configurations of the three assemblies for the case of $k_N = 10^8$ are shown in Figure 4.3.

In all cases, we note the following observations. For a particular assembly, the macroscopic deviatoric stress reaches a constant value that is independent of the elastic properties while the rate of volumetric strain tends to zero, in agreement with standard continuum plasticity theories. Comparing across the three assemblies with different particle angularity levels, however, we observe that both the peak strength and dilatancy increase with increasing angularity, i.e., from disks to non-convex. This latter observation is consistent with experimental evidence of increased strength with increasing angularity of the particles [1].

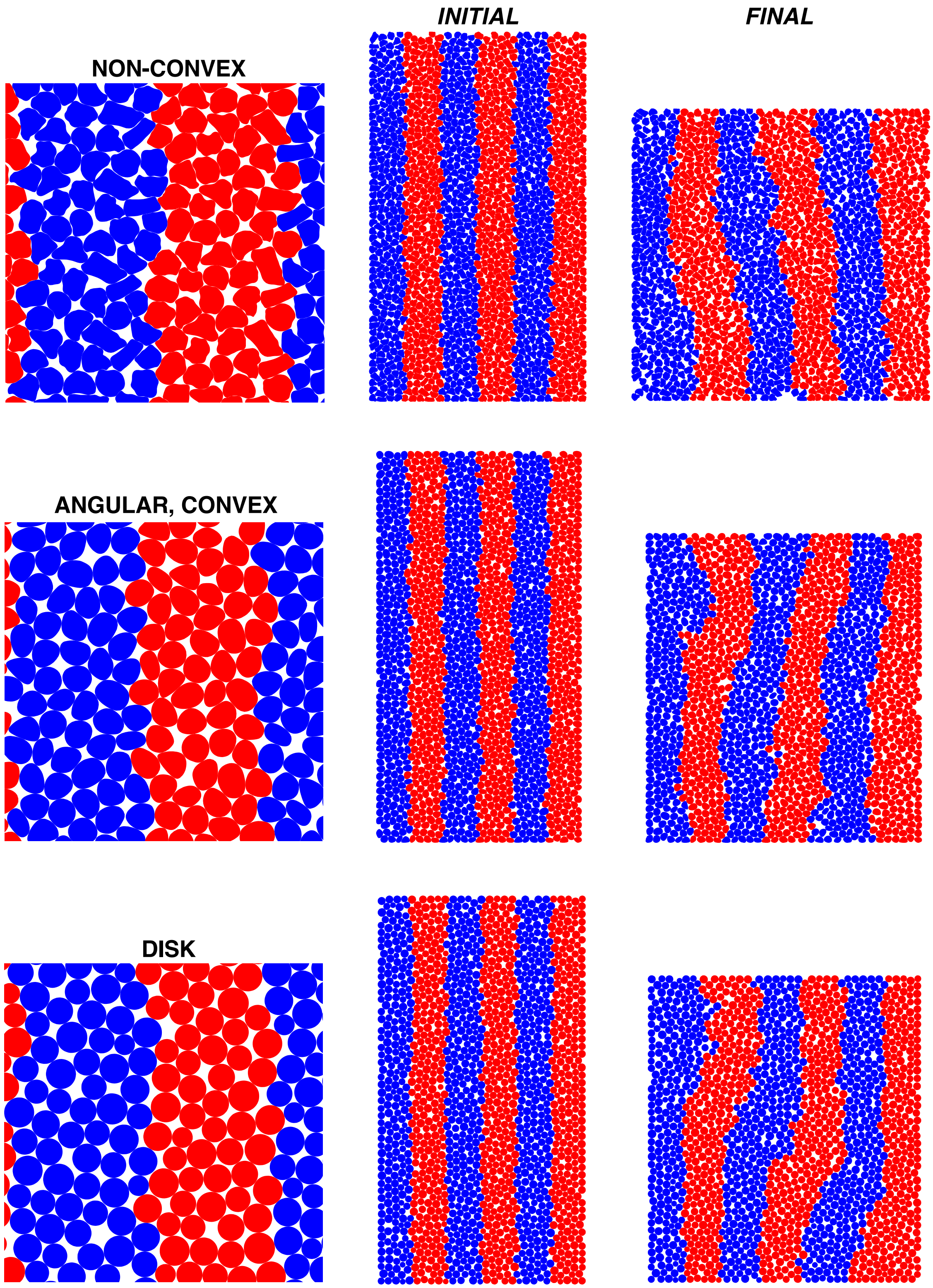

Figure 4.3: Biaxial compression: initial and final ($\epsilon_a = 0.21$) configurations with $k_N = 10^8$.

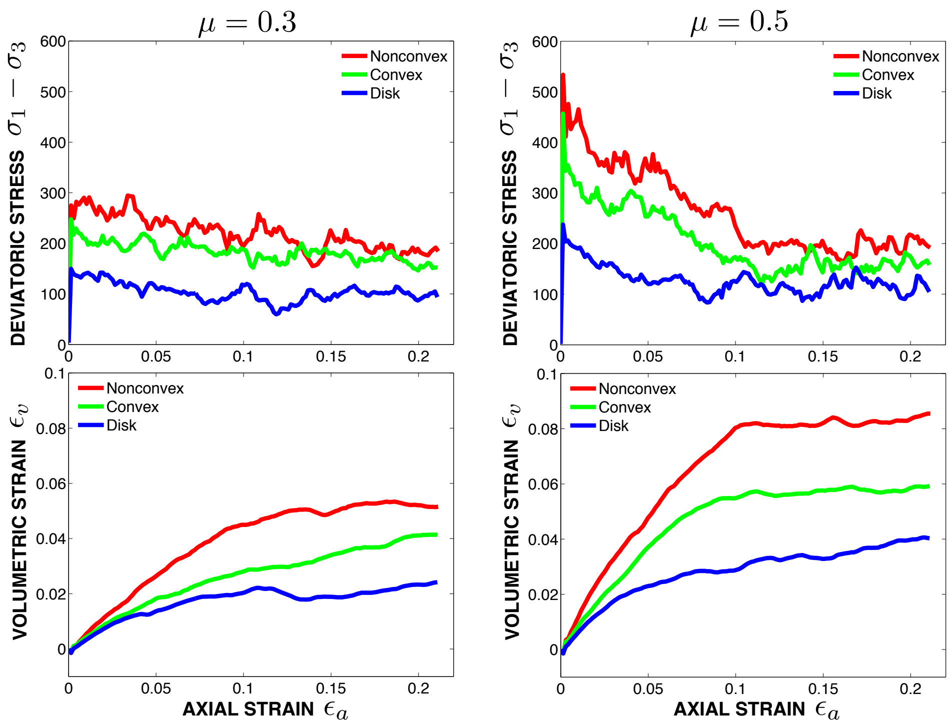

Figure 4.4: Biaxial compression: response with $k_N = \infty$.

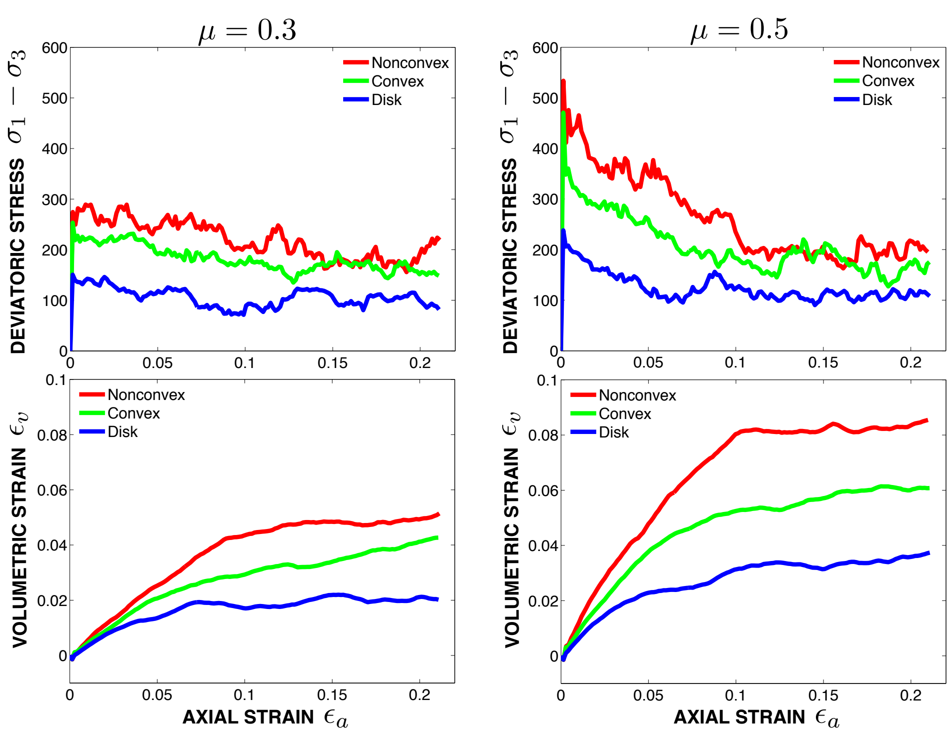

Figure 4.5: Biaxial compression: response $k_N = 10^8$.

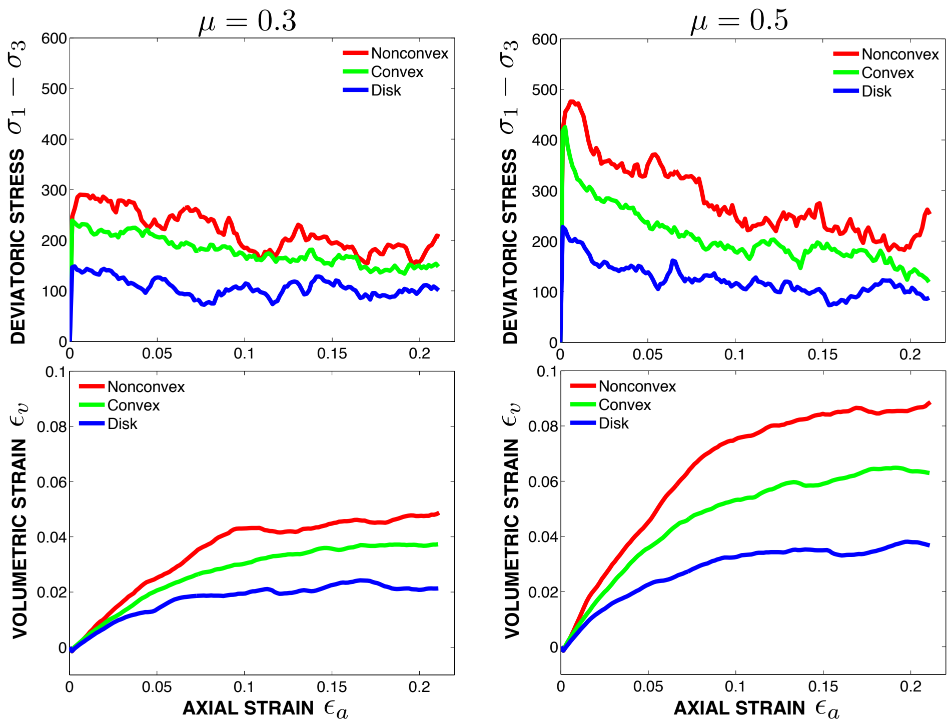

Figure 4.6: Biaxial compression: response $k_N = 10^6$.

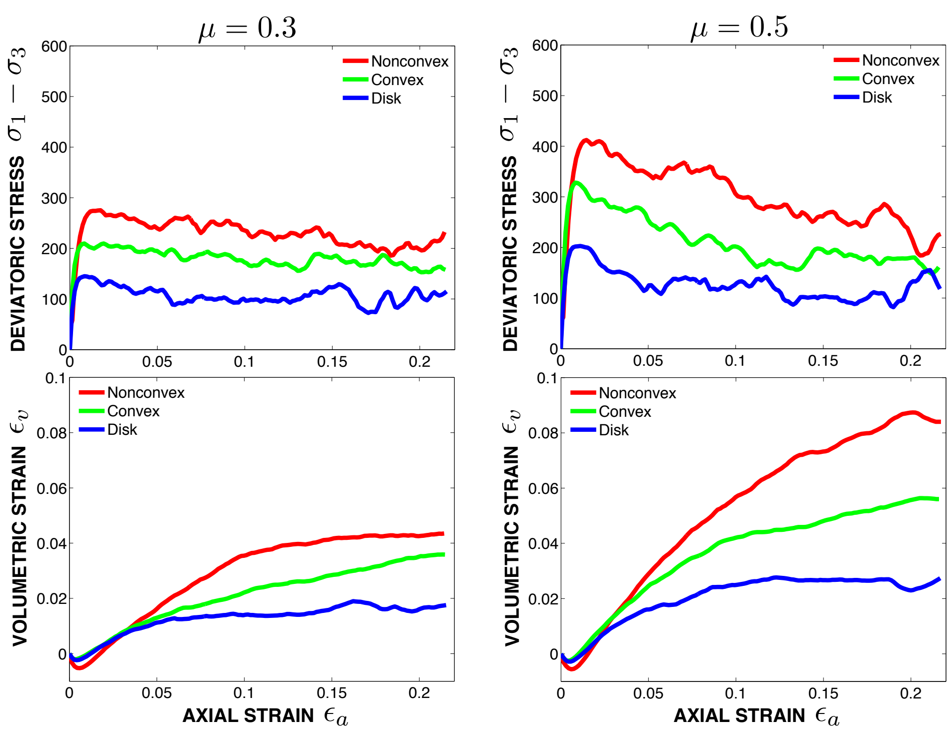

Figure 4.7: Biaxial compression: response $k_N = 10^5$.

4.4.2 Column drop test

We consider a column with an initial height to width ratio H_0/L_0 of approximately 1.68. The base supporting the column has a friction coefficient of $\mu_{\text{base}} = 0.5$, while a smooth vertical wall representing a symmetry boundary is placed on one side of the column. Three columns with 1520 particles of increasing angularity — disk, angular but convex, and non-convex, as shown at Step 0 in Figures 4.8 and 4.9 — are constructed using particles from the sixteen different shapes described in the biaxial test example. These particles are dropped into the rectangular box that forms the column and settled under gravity. Drop test simulations are then conducted by removing one of the side walls of the box and letting the column spread under gravity. The simulations are carried out using the dynamic formulation in equation (4.15) with $\theta = 0.7$ and a time step of $\Delta t = 0.05$ for two interparticle friction coefficients $\mu = 0.5$ and $\mu = 0$. We set the contact elasticity to be $k_N = 10^8$ and $k_T = 2k_N/3$ for all columns.

We compare the response evolutions of the angular and disk columns against the non-convex column, as shown in Figures 4.8 and 4.9. The final configurations of the three columns for $\mu = 0.5$ are shown in Figure 4.10. The slopes of the final spreads of the angular and disk columns are approximately 12° and 9°, respectively. More prominently, the slope in the non-convex column is 17°. This is a 5° and 8° increase from the angular and disk columns, respectively, which is quite significant. Relative to the non-convex column, the final spreads of the angular and disk columns are approximately 14 and 45 percent wider. These observations are consistent with the increase of rolling resistance with increasing angularity.

For the case of $\mu = 0$, the response evolutions of the angular and disk columns as compared with the non-convex column are shown in Figures 4.11 and 4.12, with the final configurations of all columns shown in Figure 4.13. At Step 3200, the angular and non-convex columns have stopped flowing, while the disk column continues to flow and, as the simulation is progressed, a final layer thickness of 1 particle is reached. Essentially, without rolling resistance, the disk column simply 'melts' away. On the other hand, the angular and non-convex columns maintain a well-defined spread, even at zero interparticle friction, due to the rolling resistance provided by angular and non-convex particles. As expected, the non-convex column has a smaller spread due to increased angularity in the non-convex particles.

4.5 Closure

We have presented a contact dynamics (CD) approach to our NURBS-based discrete method. By combining particle shape flexibility, properties of implicit time integration (e.g., larger time steps) and non-penetrating constraints, as well as a reduction to a static formulation in the limit of an infinite time step, we target system properties and deformation regimes in which the classical discrete element method either performs poorly or simply fail, i.e., in granular systems composed of rigid or highly stiff angular particles and subjected to quasi-static or dynamic flow conditions. The implementation the combined approach is made simple by adopting a variational framework, which enables the resulting discrete model to be readily solved using off-the-shelf mathematical programming solvers.

Numerical simulations of the biaxial compression and column drop tests for varying contact elasticities, including the rigid case, were performed, and the ability of the combined approach to capture the effects of increased rolling resistance, associated with increased angularity in and interlocking between non-convex particles, on the macroscopic response were clearly demonstrated. These effects are manifested macroscopically through an increase in the mobilized shear strength and dilatancy under biaxial compression, and a smaller spread and higher angle of response under a column drop test. These observations are consistent with reported experimental observations. The effect of geometrical bias from the use of disks to match average particle diameter on packing porosity, which in turn affects mobilized strength, is also noted.

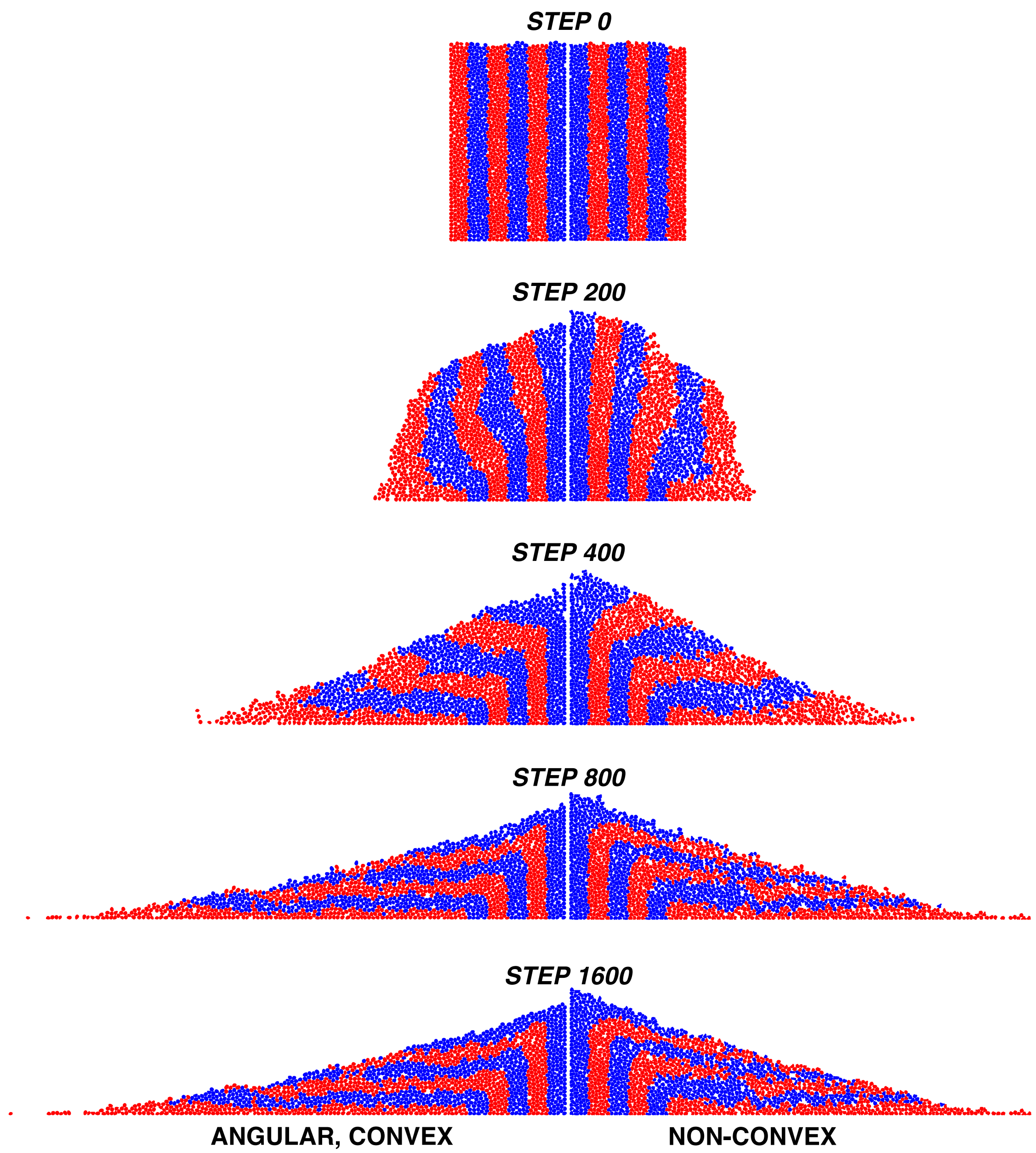

Figure 4.8: Column drop test with interparticle friction coefficient of $\mu = 0.5$: comparison between non-convex and angular particles.

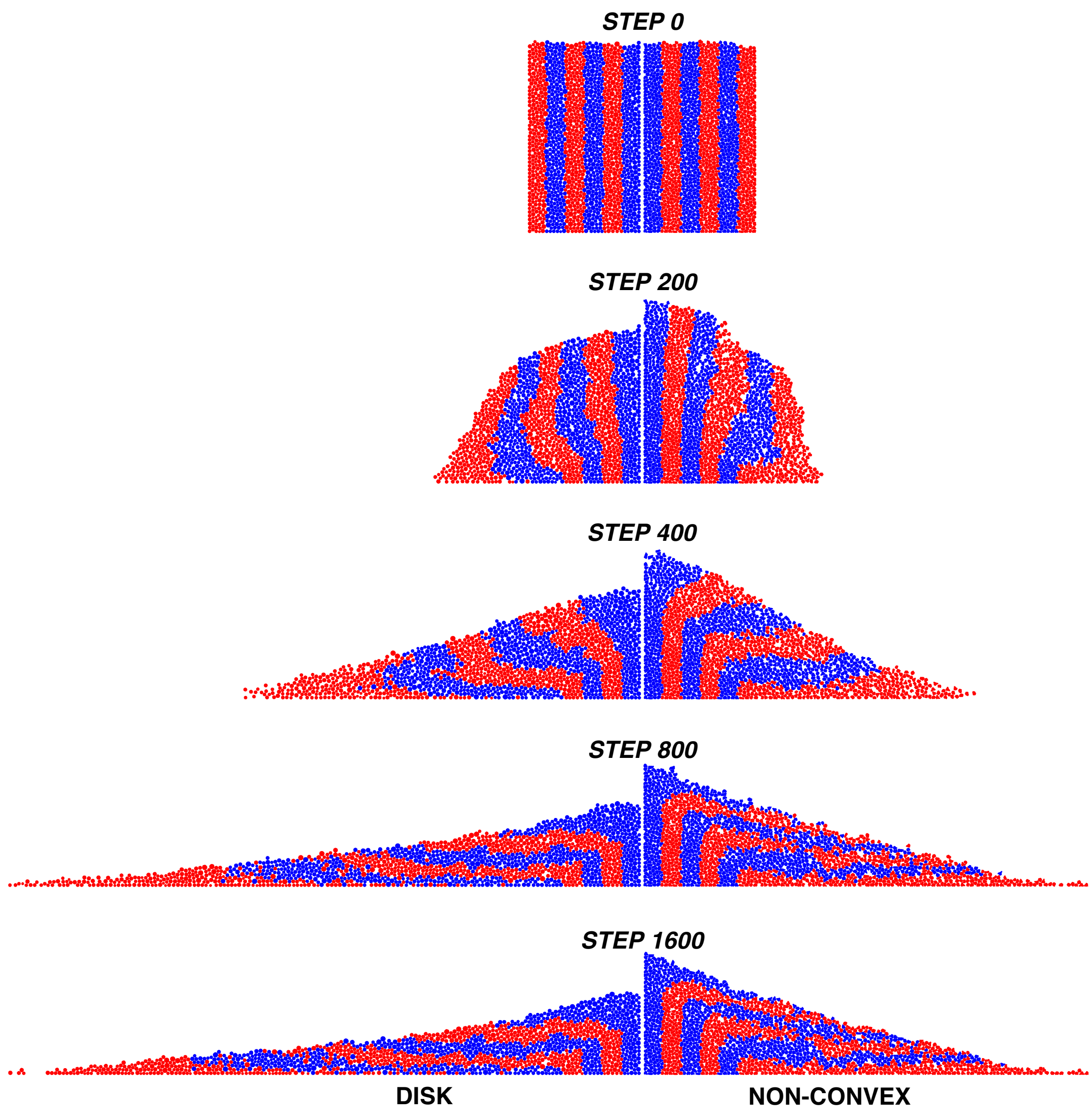

Figure 4.9: Column drop test with interparticle friction coefficient of $\mu = 0.5$: comparison between non-convex and disk particles.

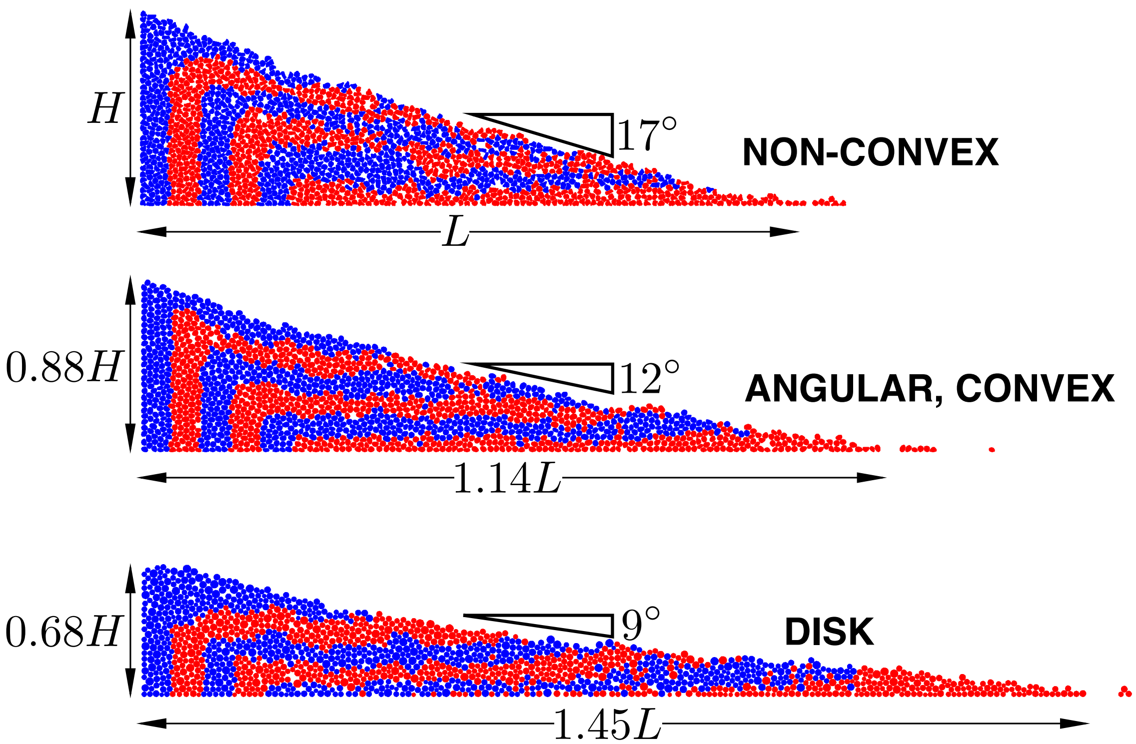

Figure 4.10: Configurations of columns with interparticle friction coefficient of $\mu = 0.5$ at step 1600: approximate dimensions relative to column with non-convex particles.

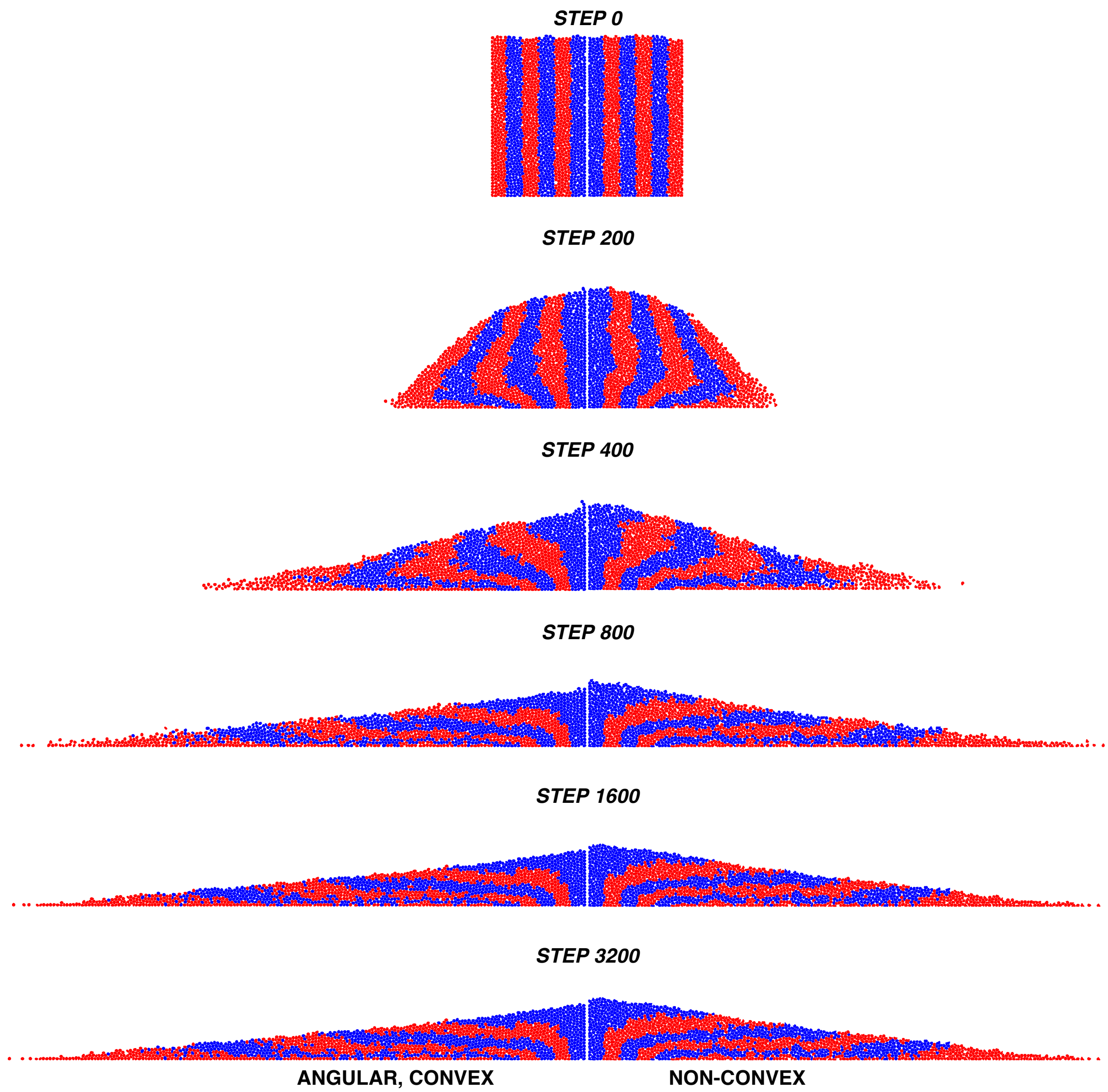

Figure 4.11: Column drop test with interparticle friction coefficient of $\mu = 0$: comparison between non-convex and angular particles.

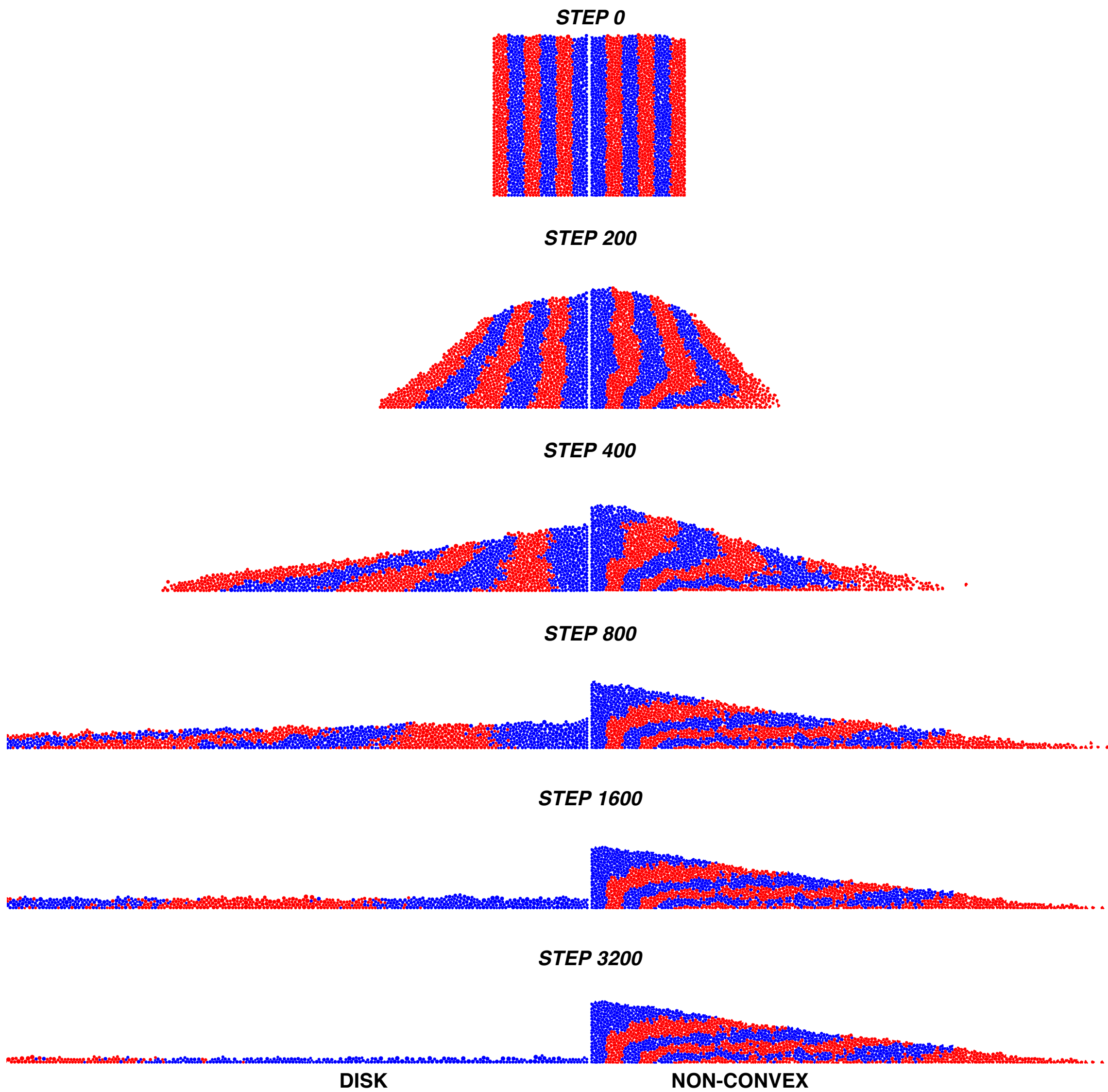

Figure 4.12: Column drop test with interparticle friction coefficient of $\mu = 0$: comparison between non-convex and disk particles. We note that at step 3200, the column with disk particles continues to flow; a final layer thickness of 1 particle is reached as the simulation is progressed.

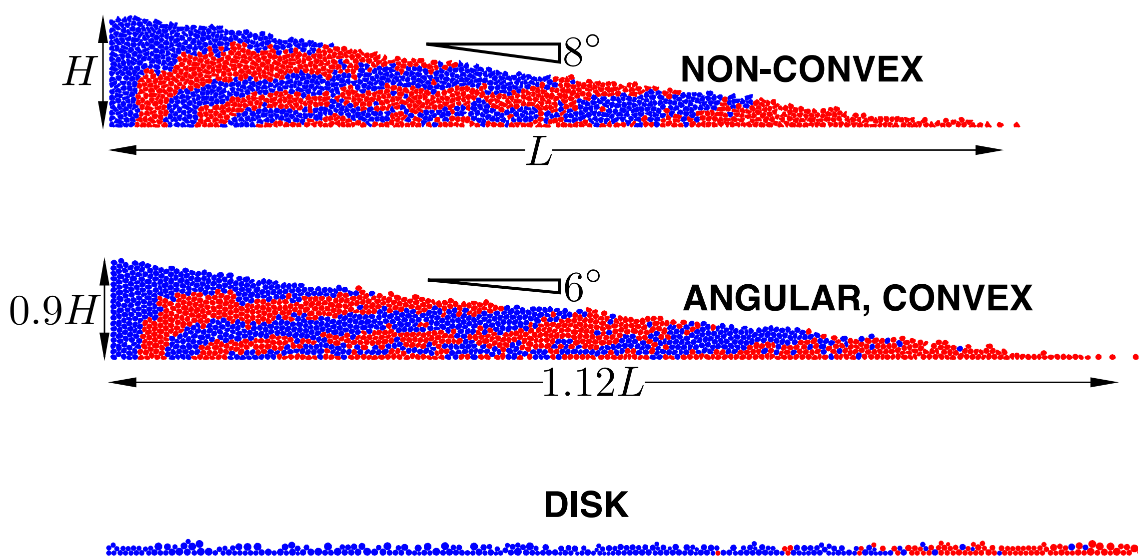

Figure 4.13: Configurations of columns with interparticle friction coefficient of $\mu = 0$ at step 3200: approximate dimensions relative to column with non-convex particles. We note that at this point in time the column with disk particles continues to flow; a final layer thickness of 1 particle is reached as the simulation is progressed.